Universal zero-bias conductance through a quantum wire side-coupled to a quantum dot

A. C. Seridonio,[1,*] M. Yoshida,[2] and L. N. Oliveira[1]
[1]*Departamento de Física e Informática, Instituto de Física de São Carlos, Universidade de São Paulo, 369 São Carlos, SP, Brazil*
[2]*Departamento de Física, Instituto de Geociências e Ciências Exatas, Universidade Estadual Paulista, 13500 Rio Claro, SP, Brazil*
(Received 16 July 2009; published 16 December 2009)

A numerical renormalization-group study of the conductance through a quantum wire containing noninteracting electrons side-coupled to a quantum dot is reported. The temperature and the dot-energy dependence of the conductance are examined in the light of a recently derived linear mapping between the temperature-dependent conductance and the universal function describing the conductance for the symmetric Anderson model of a quantum wire with an embedded quantum dot. Two conduction paths, one traversing the wire, the other a bypass through the quantum dot, are identified. A gate potential applied to the quantum wire is shown to control the current through the bypass. When the potential favors transport through the wire, the conductance in the Kondo regime rises from nearly zero at low temperatures to nearly ballistic at high temperatures. When it favors the dot, the pattern is reversed: the conductance decays from nearly ballistic to nearly zero. When comparable currents flow through the two channels, the conductance is nearly temperature independent in the Kondo regime, and Fano antiresonances in the fixed-temperature plots of the conductance as a function of the dot-energy signal interference between them. Throughout the Kondo regime and, at low temperatures, even in the mixed-valence regime, the numerical data are in excellent agreement with the universal mapping.

DOI: 10.1103/PhysRevB.80.235318 PACS number(s): 73.21.La, 72.15.Qm, 73.23.Hk

I. INTRODUCTION

The physics of nanostructured devices displays many facets. Among the most interesting ones, interference ranks high, because it is controllable, challenges classical intuition and adds colorful features to experimental plots. Iconic as the Aharonov-Bohm setup is in this context,[1–6] a great deal of attention has been given to a more elementary interferometric geometry: a quantum wire side coupled to a quantum dot.[1,7–16] An infinitesimal bias applied to the noninteracting electron gas in the quantum wire is sufficient to induce a current.

The dynamics of this *T*-shaped device parallels that of a single-electron transistor, the alternative arrangement that embeds the dot in the conduction path.[17] Either in the embedded or in the side-coupled geometry, the dot occupancy n_d is controlled by a gate potential V_d. For odd n_d, the dot magnetic moment interacts antiferromagnetically with the wire electrons. At sufficiently low temperatures, the quantum dot is shrouded by a Kondo cloud. The Kondo cloud can either favor or impede conduction, depending on the geometry. In the embedded arrangement, the strong coupling between the conduction and the dot electrons overcomes the Coulomb blockade and allows conduction. The conductance is enhanced at low temperatures. In the particle-hole symmetric limit, an early numerical renormalization group (NRG) study showed that the conductance is a monotonically decreasing universal function $G^S(T/T_K)$ of the temperature scaled by the Kondo temperature.[18]

In the side-coupled geometry, by contrast, the cloud obstructs transport along the segment of the quantum wire next to the dot. In the simplest *T*-shaped device, the conductance decays from nearly ballistic to nearly zero as the system is cooled below the Kondo temperature T_K. More elaborate *T*-shaped setups accommodate an alternative conduction path through the quantum dot, a detour around the blocked wire segment.[12,13,19] While the conductance through the wire grows with the temperature, the dot bypass faces the Coulomb blockade at high temperatures and becomes conducting at low temperatures. Thus, if the experimental conditions let the wire path overwhelm the bypass, the conductance G through the device will rise with the temperature, defining a *wirelike* thermal dependence $G_w(T)$. In the opposite extreme, the dominance of the bypass defines a *dotlike* decaying function $G_d(T)$. When the tunneling probabilities along the two paths are comparable, constructive and destructive patterns emerge in the conductance profile, i.e., in the fixed-temperature plot of the conductance as a function of the gate potential V_d. A recent experimental study has shown that a gate voltage applied to the wire at low temperatures can turn a low-conductance (i.e., wirelike) uniform profile first into a succession of destructive and constructive interferences; and then into a high-conductance (i.e., dotlike) uniform profile.[19]

Theoretical studies of the side-coupled geometry have explained a number of the features of the conductance profiles,[1,9–11,20] and computations of the temperature-dependent conductance have also been reported.[6,15,20] Recently, we have derived a universal expression mapping the Kondo-regime conductance $G(T/T_K)$ of the *T*-shaped device onto Costi's, Hewson's, and Zlatic's[18] universal function $G^S(T/T_K)$.[21] The mapping is linear. It shows that $G(T/T_K)$ is a linear combination of the dotlike conductance $G_d(T/T_K) = G^S(T/T_K)$ with the wirelike conductance $G_w(T/T_K) = \mathcal{G}_2 - G_d(T/T_K)$, where $\mathcal{G}_2 \equiv 2e^2/h$ is the quantum conductance. The linear coefficients are trigonometric functions of the ground-state phase shift δ imposed on the conduction electrons by the gate potential applied to the wire and the coupling to the quantum dot. When the phase shift increases from zero to $\pi/2$, the linear combination changes from $G(T/T_K) = G_d(T/T_K)$ to $G(T/T_K) = G_w(T/T_K)$.

This paper proposes to show that the mapping reproduces the conductance profiles, the temperature-dependent conductances, the emergence of destructive and of constructive in-

terference, the change from wirelike to dotlike behavior—all the above-described features of the experimental plots. To this end we will present essentially exact numerical renormalization group results for the conductance of the T-shaped device as a function of the temperature and dot gate potential for various gate potentials applied to the wire. The mapping to the universal function $G^S(T/T_K)$ describes accurately each calculated temperature-dependent conductance in the Kondo regime and thus condenses in a simple expression the rich variety resulting from the competition and interference between the two conduction paths in the side-coupled geometry.

This paper belongs to a triplet dedicated to the conductance for the Anderson model of a wire coupled to a quantum dot. Reference 22 discussed the embedded geometry, the first part of the paper having derived the mapping between the conductance and the universal function $G^S(T/T_K)$, and the second presenting NRG data to illustrate and to probe the accuracy of that mapping at the limits of the Kondo regime and beyond them. Reference 21 related the conductance for the T-shaped device and the universal function $G^S(T/T_K)$ and showed that the mapping affords quantitative agreement with experimental data reported in Refs. 13 and 19. Here, we compare that analytical expression with essentially exact NRG results for the conductance in the Kondo regime and in the adjacent mixed-valence regimes.

Our presentation is divided in five sections. Section II defines the model Hamiltonian and recalls basic concepts associated with it. The mapping is discussed in Sec. III. A comprehensive overview of the numerical results follows (Secs. IV and V), including the comparison with the mapping to the universal function. Finally, Sec. VI summarizes our conclusions.

II. MODEL

The overview of the numerical results in Secs. IV and V will divide the parametrical space of the model in a number of regimes, easily identified by their nearly uniform conductances. Before examining the NRG results, it is therefore convenient to discuss the characteristic energies staking the boundaries of those regimes. This section defines the model Hamiltonian, relates the conductance to its eigenvalues and eigenvectors, and refers to the pioneer investigations that led to the characteristic scales in its spectrum.[23–25]

A. Hamiltonian

The quantum dot in Fig. 1 is side coupled to a quantum wire. Gate potentials V_d and V_w control the occupations of the dot and of the Wannier orbital

$$f_0 \equiv \frac{1}{\sqrt{N}} \sum_k a_k. \tag{1}$$

Current flows in response to a bias voltage. In standard notation, the Anderson Hamiltonian capturing the physics of this setup is

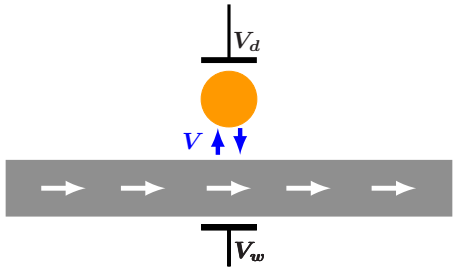

FIG. 1. (Color online) T-shaped device. The circle depicts a quantum dot side-coupled to a quantum wire. The gate potentials V_d and V_w control the electronic occupations of the dot and of the Wannier orbital (1), respectively. The device allows interference between the current flowing along the primary conduction path, indicated by the white arrows, and the electrons that bypass the central portion of the wire by way of the dot.

$$H_A = \sum_k \epsilon_k a_k^\dagger a_k + W f_0^\dagger f_0 + V(f_0^\dagger c_d + \text{H.c.}) + H_d. \tag{2}$$

The first term on the right-hand side defines a noninteracting, structureless half-filled conduction band of half-width D. The second term introduces a scattering potential W, controlled by the gate voltage V_w, and the tunneling amplitude V couples the spin-degenerate dot level c_d to the f_0 orbital.

The dot Hamiltonian H_d in Eq. (2) can be written as

$$H_d = \left(\varepsilon_d + \frac{U}{2}\right) n_d - \frac{U}{2} n_{d\uparrow} n_{d\downarrow}, \tag{3}$$

which defines the antisymmetric component $\varepsilon_a \equiv \varepsilon_d + U/2$ of the dot energy, i.e., the component that changes sign under the particle-hole transformation $c_d \to -c_d^\dagger$, $a_k \to a_k^\dagger$.

The second term on the right-hand side of the Eq. (3), by contrast, remains invariant under the same transformation. For $W = \varepsilon_a = 0$, the Anderson Hamiltonian reduces to the symmetric Hamiltonian H_A^S.

B. Conductance

A detailed derivation of an equation for the electrical conductance $G(T)$ at the temperature T in the embedded configuration was presented in Ref. 22. In the side-coupled configuration of Fig. 1, the same analysis leads to an analogous expression,

$$G(T) = \mathcal{G}_2 \frac{\beta\pi\Gamma}{\mathcal{Z}} \sum_{mn} \frac{|\langle m|f_0|n\rangle|^2}{e^{\beta E_m} + e^{\beta E_n}}, \tag{4}$$

where $\mathcal{G}_2 \equiv 2e^2/h$ is the quantum conductance, $\mathcal{Z}$ is the partition function, $|m\rangle$ ($|n\rangle$) is an eigenstate of H_A, with eigenvalue E_m, and $\Gamma \equiv \pi\rho V^2$ is the dot-level width, due to its coupling to the quantum wire.

C. Characteristic energy scales

The characteristic energies in the spectrum of the Hamiltonian (2) are depicted by Fig. 3 in Ref. 22. The dot Hamiltonian (3) introduces the excitation energy $\Delta_0 = -\varepsilon_d$ ($\Delta_2 = U + \varepsilon_d$) necessary to remove an electron from (add an electron

to) the singly-occupied level. The conduction band Hamiltonian contributes only a trivial energy scale, the half-width D, but its coupling to the dot adds two energies to the collection: the level width Γ and the Kondo energy $k_B T_K$. The scattering potential W reduces the former to[22]

$$\Gamma_w = \frac{\pi\rho V^2}{1+(\pi\rho W)^2}. \tag{5}$$

A side effect of the coupling, emergent in the spectrum of particle-hole asymmetric Hamiltonians, is the renormalization $\Delta_0 \to \Delta_0^*$, or $\Delta_2 \to \Delta_2^*$, of the lowest dot-excitation energy.[23,25] Apart from displacing the Kondo regime,[22] this energy shift has no practical consequence.

The Kondo regime is defined by the condition $\max(k_B T, \Gamma_w) \ll \mathcal{E}_c^K$, where the dominant characteristic energy is $\mathcal{E}_c^K = \min(D, \Delta_0^*, \Delta_2^*)$. The $n_d=0$ and $n_d=2$ dot configurations are then energetically inaccessible, and a dot magnetic moment arises. As the temperature is reduced below the band half-width D, the antiferromagnetic interaction between the conduction electrons and the dot electron progressively screens the moment. At low temperatures, the dot and conduction spins end up locked in a singlet. The singlet energy defines the Kondo scale $k_B T_K$.

In the parametric space of the model Hamiltonian, two mixed-valence regions enclose the Kondo regime. One of them is defined by the inequality $\Gamma_w \gtrsim \Delta_0^*$, the other, by $\Gamma_w \gtrsim \Delta_2^*$. In the mixed-valence regime the dominant characteristic energy is $\mathcal{E}_c^{mv} = \Gamma_w$, and at high temperatures, the dot moment is only partially formed. As the thermal energy is reduced past Γ_w, the dot level c_d couples strongly to the surrounding conduction electrons, and all physical properties approach their low-temperature limit.

III. UNIVERSAL MAPPING

The derivation of the universal expression mapping the conductance in Eq. (4) to the universal function $G^S(T/T_K)$ computed by Costi, Hewson, and Zlatic[18,26] has been summarized elsewhere.[21] A detailed presentation of the analogous derivation for the single-electron transistor being moreover available,[22] only recapitulation of the central result is required,

$$G\left(\frac{T}{T_K}\right) - \frac{\mathcal{G}_2}{2} = \left[G^S\left(\frac{T}{T_K}\right) - \frac{\mathcal{G}_2}{2}\right]\cos(2\delta). \tag{6}$$

Here, δ is the ground-state phase shift of the conduction electrons in the wire.

To bring out the physical content of Eq. (6), we rewrite it in the equivalent form

$$G\left(\frac{T}{T_K}\right) = G^S\left(\frac{T}{T_K}\right)\cos^2\delta + \left[\mathcal{G}_2 - G^S\left(\frac{T}{T_K}\right)\right]\sin^2\delta, \tag{7}$$

which shows that the conductance is a linear combination of the universal function $G^S(T/T_K)$ with its complement, $\mathcal{G}_2/2 - G^S(T/T_K)$. The universal function $G^S(T/T_K)$, a monotonically decreasing function of T/T_K that describes the conductance through a particle-hole symmetric quantum dot in the embedded configuration, is the dotlike function G_d discussed in the introduction, while its complement, a monotonically increasing function of T/T_K that describes the conductance through a particle-hole symmetric quantum dot in the side-couple configuration, is the wirelike function G_w. If the two conduction paths were independent, the resultant conductance would be the sum $G_d(T/T_K) + G_w(T/T_K) = \mathcal{G}_2$; the coefficients $\cos^2\delta$ and $\sin^2\delta$ account for the interference between the two currents.

Special limits

Four limits of Eq. (6) merit special attention. For $\delta = \pi/2$, the mapping reduces to

$$G\left(\frac{T}{T_K}\right) = \mathcal{G}_2 - G^S\left(\frac{T}{T_K}\right) \quad (\delta = \pi/2). \tag{8a}$$

This result can be derived from a diagrammatic expansion for the symmetric Anderson Hamiltonian.[11,22] With $\delta = \pi/2$, an equality approximately satisfied throughout the Kondo regime for $W=0$,[22] the conductances for the side-coupled and the embedded geometries are complementary. While the conductance through the single-electron transistor rises from nearly zero to ballistic across the Kondo crossover, the conductance through the T-shaped device decays from ballistic to nearly zero.

Physically, Eq. (8a) is readily understood. At high temperatures, the flow of electrons through the quantum wire in Fig. 1 is independent of the weak coupling to the quantum dot. As the temperature is reduced, however, the formation of the Kondo cloud gradually blocks the flow, and the conductance decays in the same way that the conductance through an embedded quantum dot would rise.

In the second special limit, $\delta=0$, Eq. (6) yields

$$G\left(\frac{T}{T_K}\right) = G^S\left(\frac{T}{T_K}\right) \quad (\delta = 0). \tag{8b}$$

To satisfy the Friedel sum rule,[27] the phase shift tends to approach $\pi/2$ at low temperatures; to make it vanish, a strong wire potential W is required. The potential affects the conductance in two different ways: it induces a charge that blocks transport through the central region of the wire; at the same time, it opens a bypass through the quantum dot. At high temperatures, the bypass is ineffective because the Coulomb blockade impedes conduction through the dot. Upon cooling, the Kondo effect raises the blockade and the conductance rises, lifted by the very same mechanism that allows conduction in a single-electron transistor.[17,28,29]

The third simple limit of Eq. (6) is $G(T=0)$. At low temperatures, the universal curve G^S approaches $\mathcal{G}_2$. From Eq. (6), it follows that

$$G(T) = \mathcal{G}_2 \cos^2\delta \quad (T \ll T_K), \tag{8c}$$

a result most easily obtained from Langreth's relation[27] between the low-energy dot-level spectral density and the ground-state phase shift.[21]

Finally, at high temperatures, the universal function G^S vanishes, and Eq. (6) yields

$$G(T) = \mathcal{G}_2 \sin^2 \delta \quad (T \gg T_K), \tag{8d}$$

Analogous to Eq. (8c), this result also stems from Langreth's expression. In the temperature range $k_B T_K \ll k_B T \ll \mathcal{E}_c^K$ within the Kondo regime, the Anderson Hamiltonian is in the local-moment regime, equivalent to a phase-shifted conduction band weakly interacting with the dot moment.[24] If the interaction is neglected, the Hamiltonian is equivalent to a free conduction band, and Langreth's relation is applicable.[21,22] The phase shift δ_{LM} of the wire electrons can be obtained from the Friedel sum rule, which associates a phase-shift difference $\pi/2$ with the formation of the Kondo cloud, and hence yields $\delta_{LM} = \delta - \pi/2$. Substitution of δ_{LM} for δ in Eq. (8c) leads to Eq. (8d).

IV. NUMERICAL RESULTS

We are now ready to discuss the NRG results and compare them with Eq. (6). Details of the numerical procedure yielding the ground-state phase shift δ and the temperature-dependent conductance $G(T)$, and a tabulation of the parameters controlling the accuracy of the computation are found in one of our earlier papers.[22] Here, to follow the structure of that report, we discuss two Coulomb repulsions: $U=5D$, in Sec. IV A, and $U=0.05D$, in Sec. IV B.

Although the latter choice can be more faithful to experimental conditions, the former is more illustrative. With $U > D$, the inequality $k_B T \ll \min D, |\varepsilon_d|, \varepsilon_d + U$, which defines the thermal dimension of the Kondo regime, reduces to $k_B T \ll D$. With $U=5D$, the domain of Eq. (6) will cover all but a small portion of our $\log(k_B T/D)$ axes. For this reason, we pay closer attention to the larger Coulomb repulsion.

A. Results for $U > D$

1. Phase shifts

Figure 2 shows the ground-state phase shifts extracted from the low-energy spectrum of the Hamiltonian H_A for antisymmetric dot energies $\varepsilon_a \equiv \varepsilon_d + U/2$ for $|\varepsilon_a| < 3.5D$. It follows from the Friedel sum rule that the ordinate $2\delta/\pi$ is the extra charge n_w at the wire. That accumulation is the sum of two charges: that induced by the wire potential W; and the Kondo screening charge, which is equal to the dot occupation n_d.

With $W=0$, the two occupations are equal and bound between $n_w = n_d = 0$ and $n_w = n_d = 2$. If, in addition, $\varepsilon_a = 0$, H_A reduces to the symmetric Hamiltonian; the dot occupation is unitary, and $\delta = \pi/2$. If, on the other hand, $\varepsilon_a \neq 0$, then a particle-hole transformation, which reverses the sign of ε_a, transmutes n_d into $2 - n_d$ and hence, as illustrated by the circles in Fig. 2, changes the sign of $\delta - \pi/2$. The solid line through the circles marks the Kondo regime, throughout which $\delta \approx \pi/2$. Comparison with the solid lines through the squares and triangles shows that the positive gate potential applied to the wires displaces the Kondo regime to higher dot energies.

The negative charge induced by the potential pushes down the entire curve. For $\varepsilon_d > 0$, the wire charge n_w now becomes negative. While the circles cross the $\delta = \pi/2$ line at a saddle point, the slope of the curves through the squares and triangles is markedly negative. Thus, in contrast with the circles, only in narrow ranges of dot energies do the squares and triangles dwell near $\delta = \pi/2$ or $\delta = 0$. As the data also show, except for $W \approx 0$, the range in which $\delta \approx 0$ ($\delta \approx \pi/2$) is pinned to the vicinity of the mixed-valence region $\varepsilon_a \approx U/2$ ($\varepsilon_a \approx -U/2$).

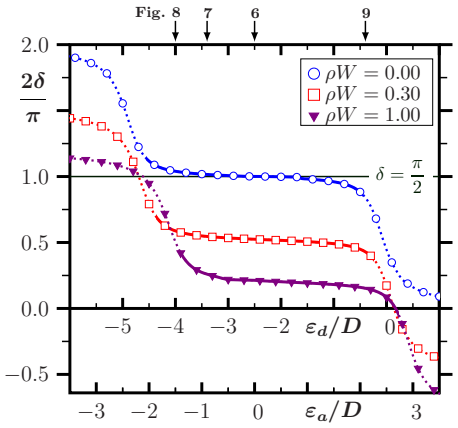

FIG. 2. (Color online) Phase shifts as functions of the dot-level energy for the indicated wire potentials W. The triangles, squares, and circles were obtained from the low-energy fixed-point Hamiltonian for $U=5D$ and $\Gamma_w = 0.15D$. For each curve, a solid line guides the eyes through the data points in the pertinent Kondo regime. The horizontal line labeled $\delta = \pi/2$ identifies the dot energies at which the right-hand side of Eq. (8c) vanishes. The vertical arrows pointing to the top axis indicate the dot energies at which the temperature-dependent conductance is shown in Figs. 6–9.

Combined with Eq. (6), the information in Fig. 2 determines the thermal dependence of the conductance through the device in Fig. 1. Preliminary to comparing quantitatively that equality with the NRG results for $G(T)$, in Secs. IV A 1–IV A 4 we present bird's-eye views of the conductance as a function of the temperature and dot-level energy.

2. Conductance for $W=0$

Figure 3 combines 71 $G(T)$ curves calculated for $W=0$, $U=5D$, $\Gamma_w = 0.15D$, and dot energies in the range focused in Fig. 2. The inset shows a reversed-perspective view of the same plot. From our discussion of Eqs. (8), the salient features of the landscape are readily recognized. The central portion of the plot encompasses the Kondo regime. Here, as the circles in Fig. 2 show, the ground-state phase shift is close to $\pi/2$. At high temperatures, Eq. (8d) yields the nearly ballistic conductance depicted by the hoodlike central plateau in the main plot and inset. At low temperatures, Eq. (8c) brings the conductance down to nearly zero; the resulting Kondo valley is visible in the inset. We defer to Sec. IV A 5 the quantitative discussion of the crossover between the plateau and the valley. Here, we note that the Kondo temperature rises with $|\varepsilon_a|$. For $|\varepsilon_a| \approx U/2$, i.e., for $\Delta_0 \equiv -\varepsilon_d \lesssim \Gamma$ or $\Delta_2 \equiv \varepsilon_d + U \lesssim \Gamma$, the Kondo temperature becomes comparable with Γ_w, an indication that the Hamiltonian has transposed the limits of the Kondo domain to enter the mixed-valence regime.

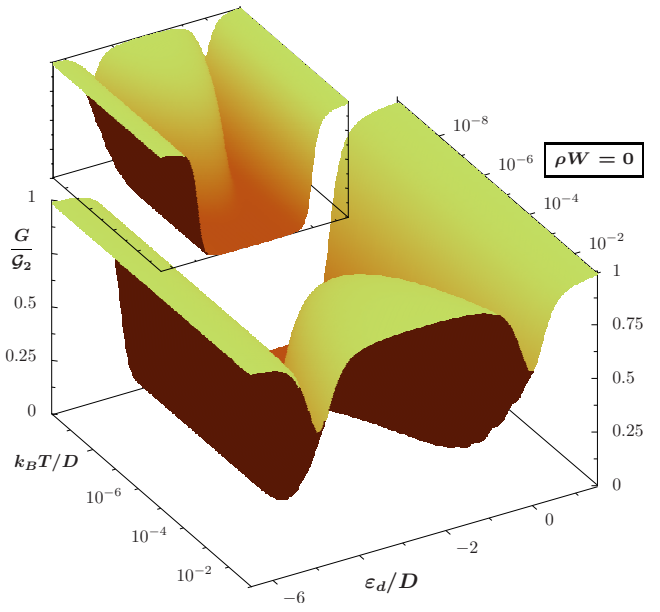

FIG. 3. (Color online) Conductance as a function of the temperature and dot-level energy for $W=0$, $U=5D$, and $\Gamma_w=0.15D$. The inset shows the same plot from the opposite viewpoint, i.e., so that, instead of rising, the temperature decays toward the viewer. The invariance of $G(T)$ under particle-hole transformations makes the plot symmetric with respect to the $\varepsilon_d=-U/2$ plane. At high temperatures in the Kondo regime, the main plot offers an unobstructed view of the high-temperature plateau, while the Kondo valley at low temperatures can only be seen in the inset. The two ridges adjacent to the Kondo regime, distinctively marked by the bell-shaped resonances at the frontal plane of the main plot belong to the mixed-valence regime. The ballistic flaps at the $\varepsilon_d=-6D$ and $\varepsilon_d=D$ ends of the landscape correspond to the dot occupations $n_d=2$ and $n_d=0$, respectively.

At high temperatures, the mixed-valence regime is identified by the two antiresonances bringing the conductance to $\mathcal{G}_2/2$ on the frontal plane of the main plot, or the rear plane of the inset. As the temperature is reduced, the conductance descends into the Kondo plateau. This decay can still be mapped onto the universal function $G^S(T/T_K)$, as Sec. IV A 5 will show. The crossover temperature is so high, however, that Eq. (6) fits quantitatively only the low-temperature tail of the numerical results.

Beyond the mixed-valence regime, as $|\varepsilon_a|>$ grows past $U/2$, the dot occupation approaches an even integer, $n_d=0$ or $n_d=2$, the coupling to the quantum wire becomes ineffective, and the electrons flow ballistically across the wire.

3. Conductance for weak scattering potentials

Even moderate gate potentials applied to the wire change qualitatively the conductance landscape. Figure 4 shows plots analogous to Fig. 3, calculated for the same Coulomb repulsion $U=5D$ and effective dot-level width $\Gamma_w=0.15D$, for three weak potentials: (a) $\rho W=0.1D$; (b) $\rho W=0.2D$; and (c) $\rho W=0.3D$. Compared to the symmetric landscape in Fig. 3, the new plots show distinctions that evolve rapidly under the gate potential.

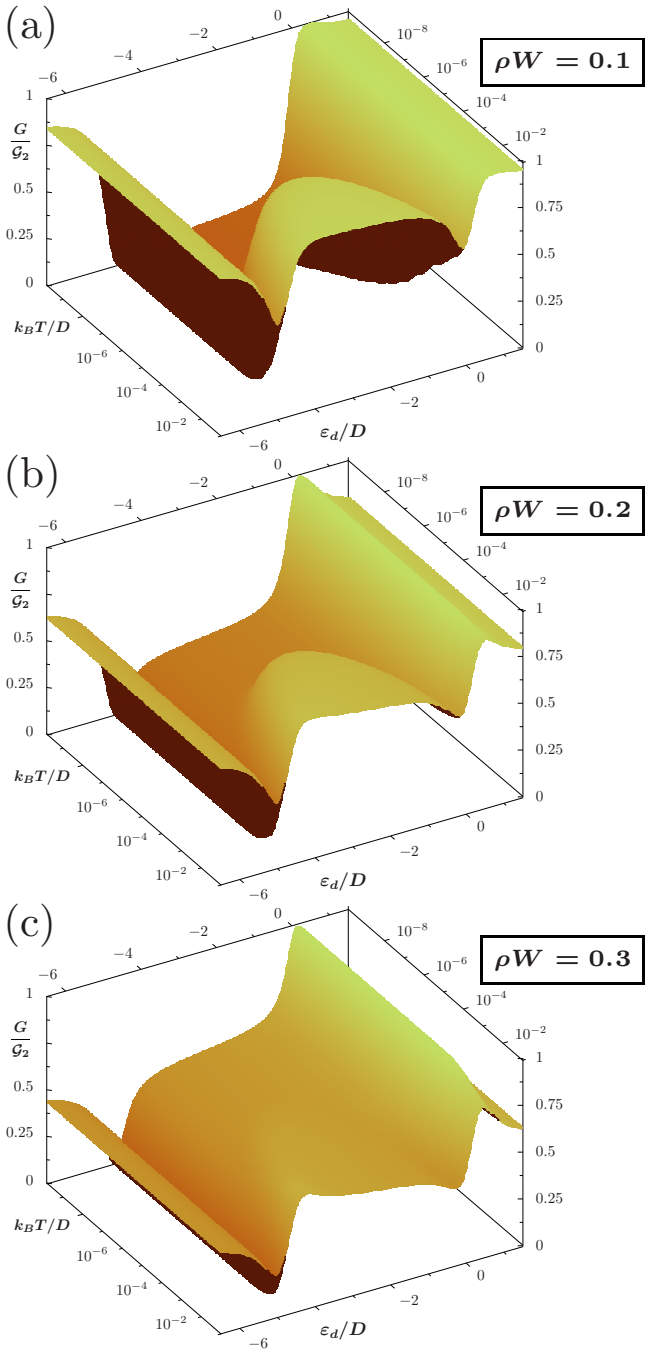

FIG. 4. (Color online) Conductance as a function of the temperature and dot-level energy for $U=5D$, $\Gamma_w=0.15D$, and the indicated wire potentials W. The wire potential reduces the conductance at the Coulomb-blockade plateau and raises the conductance in the Kondo valley. For $\rho W=0.3$, in the Kondo regime the landscape is nearly flat. The wire potential also makes the transitions into the mixed-valence regimes markedly asymmetric: at fixed temperature below $k_B T=10^{-3}D$, the conductance vanishes at the $\Delta_2^*=0$ resonance and reaches the ballistic limit at the $\Delta_0^*=0$ resonance. At low temperatures, as a result, the conductance acquires the askew profile distinctive of Kondo antiresonances.

The Kondo-valley conductance rises with ρW, while the high-temperature plateau diminishes. For the highest potential shown, $\rho W=0.3$, the conductance in the Kondo regime is

nearly uniform. Outside the Kondo regime, in the even-n_d regions, the charge $2\delta_w/\pi$ induced by the wire potential lowers the ground-state phase shift to $-\delta_w$ $(\pi-\delta_w)$ for $n_d=0$ $(n_d=2)$. The right-hand side of Eq. (8c) is no longer ballistic: $G(T=0)=\mathcal{G}_2\cos^2\delta_w$. In the mixed-valence regime, the transition from the Kondo regime to the $n_d=0$ domain is markedly different from the transition to the $n_d=2$ domain. The former encompasses the narrow $\delta=0$ dot-energy range in Fig. 2, in which the right-hand side of Eq. (8c) yields $G(T=0)\approx\mathcal{G}_2$, while the latter traverses the equally narrow $\delta=\pi/2$ range, for which Eq. (8c) yields $G(T=0)\approx 0$. An insulating gully develops in the conductance landscape, pinned near $\varepsilon_d=-U$, while a ballistic ridge arises near the $\varepsilon_d=0$ plane. Plotted at fixed temperature $k_BT\ll\Gamma_w$ against the dot energy, the conductance displays the resonance-antiresonance pair that defines a Fano profile.[30] As evidenced by Fig. 4(c), this fiducial mark of interference between currents flowing along parallel paths becomes most pronounced for intermediate wire potentials.

A brief glance at Fig. 1 identifies the interfering conduction paths. The path indicated by the white arrows may be obstructed, by charge piled up in the central segment of the wire. The second conduction path runs through the quantum dot; to bypass the obstructed wire, it must avoid the Wannier orbital f_0. At first sight, given that Eq. (2) couples the quantum dot to f_0, this may seem impossible, and in fact, with $W=0$, it is. The wire potential nonetheless spreads the coupling over wire states beyond the central Wannier orbital.

To be more specific, we let $V\to 0$ and consider the resulting wire Hamiltonian,

$$H_w=\sum_k \epsilon_k c_k^\dagger c_k+\frac{W}{N}\sum_{k,k'} c_k^\dagger c_{k'}. \tag{9}$$

The diagonalization of this quadratic form yields

$$H_w=\sum_\ell \varepsilon_\ell g_\ell^\dagger g_\ell, \tag{10}$$

where

$$g_\ell=\sum_k \alpha_{\ell,k}c_k, \tag{11}$$

with coefficients $\alpha_{\ell,k}$ that depend on W, and the eigenvalues ε_ℓ are phase shifted with respect to the ϵ_k. In the vicinity of the Fermi level, in particular, the phase shifts δ_w are uniform,

$$\tan\delta_w=-\pi\rho W. \tag{12}$$

In analogy with Eq. (1), we can therefore define

$$\phi_0\equiv\frac{1}{\sqrt{N}}\sum_\ell g_\ell. \tag{13}$$

A straightforward calculation shows that $\{\phi_0^\dagger,f_0\}=\cos\delta_w$.[22] For $W=0$, in particular, $\phi_0=f_0$. It is also easy to check that the ground-state occupation n_0 of the ϕ_0 orbital is $1+2\delta_w/\pi$, so that as required by the Friedel sum rule, the gate potential brings in an extra charge $2\delta_w/\pi$.

The operator ϕ_0 plays the role that belonged to f_0 when $W=0$. In the Kondo regime, the antiferromagnetic interaction between the dot moment and the moment of the electrons occupying the ϕ_0 orbital is now responsible for the Kondo crossover,[22,25] and at low temperatures, the ϕ_0 occupation, equal to the charge in the Kondo cloud added to the charge induced by the wire potential, obstructs the transport along the white arrows in Fig. 1. For $W\neq 0$, however, the overlap $\sin\delta_w$ between f_0 and the wire states orthogonal to ϕ_0 offers the dot bypass, through which the current runs to interfere with the flow across ϕ_0 and generate the askew profile most visible on the $k_BT=10^{-10}D$ (rear) plane in Fig. 4(c).

The ratio between the overlaps (i) $\sin\delta_w$, of f_0 with the states orthogonal to ϕ_0; and (ii) $\cos\delta_w$, of f_0 with ϕ_0, i.e., the ratio between the amplitudes for tunneling (i) through the dot and (ii) across the ϕ_0 orbital, defines the effective Fano parameter

$$q_{eff}\equiv\tan\delta_w=-\pi\rho W. \tag{14}$$

For $W=0$, the right-hand side vanishes. The resulting conductance curve, stamped on the $k_BT=10^{-10}D$ plane in Fig. 3, exhibits the symmetry of the $q=0$ Fano profile.[30] For $\rho W=0.3$, by contrast, $q_{eff}\approx -1$, and the conductance profile in Fig. 4(c) is close to the maximum Fano asymmetry.

4. Conductance for strong scattering potentials

Under stronger gate potentials, while the amplitude for conduction along the white arrows in Fig. 1 diminishes, the dot bypass becomes more effective. The absolute value of the right-hand side of Eq. (14) grows, and the conductance profile at low temperatures gradually acquires the symmetry of the large-q Fano profile.

Illustrative landscapes are displayed in Figs. 5(a)–5(c), computed for $\rho W=0.4$, 0.6, and 1.0, respectively, and $U=5D$ and $\Gamma_w=0.15D$. The dominant features of Fig. 4 reappear in the three plots. In particular, the ballistic ridge and the insulating gully are still salient in the mixed-valence regime. Sharp as they are in (a), and (b), the resonance and the antiresonance become dull in Fig. 5(c) because, as shown by the triangles in Fig. 2, the wire potential pushes $\delta(\varepsilon_d)$ so far down that the curve cuts the $\delta=\pi/2$ and $\delta=0$ horizontal lines with gentler slopes.

In the Kondo regime, while the high-temperature conductance falls, the low-temperature conductances rises steadily with ρW. In the end, with $\rho W=1$, the conductance is nearly ballistic in the low-temperature Kondo plateau, while at high temperatures the Coulomb blockade (the charge induced by the wire potential) impedes transport through the dot (through the wire) and reduces the conductance to nearly zero.

The trend in Fig. 5 indicates that, in the large ρW limit, the conductance landscape is complementary to the plot in Fig. 3, i.e., $G_{W\to\infty}(T)+G_{W=0}(T)=\mathcal{G}_2$. In view of Eq. (8a), we expect $G_{W\to\infty}(T)$ to reproduce the thermal dependence of the conductance for a single-electron transistor.[22] The comparison of Fig. 5 with Fig. 7 in Ref. 22, which describes a single-electron transistor with the same model parameters, confirms that, with $\rho W\to\infty$, the conductances in the side-coupled and the embedded configurations are identical. In the weak potential limit, on the other hand, while the conductance in the embedded configuration retains the Kondo-plateau topography in Fig. 5(c), in the side-coupled geometry the pattern is

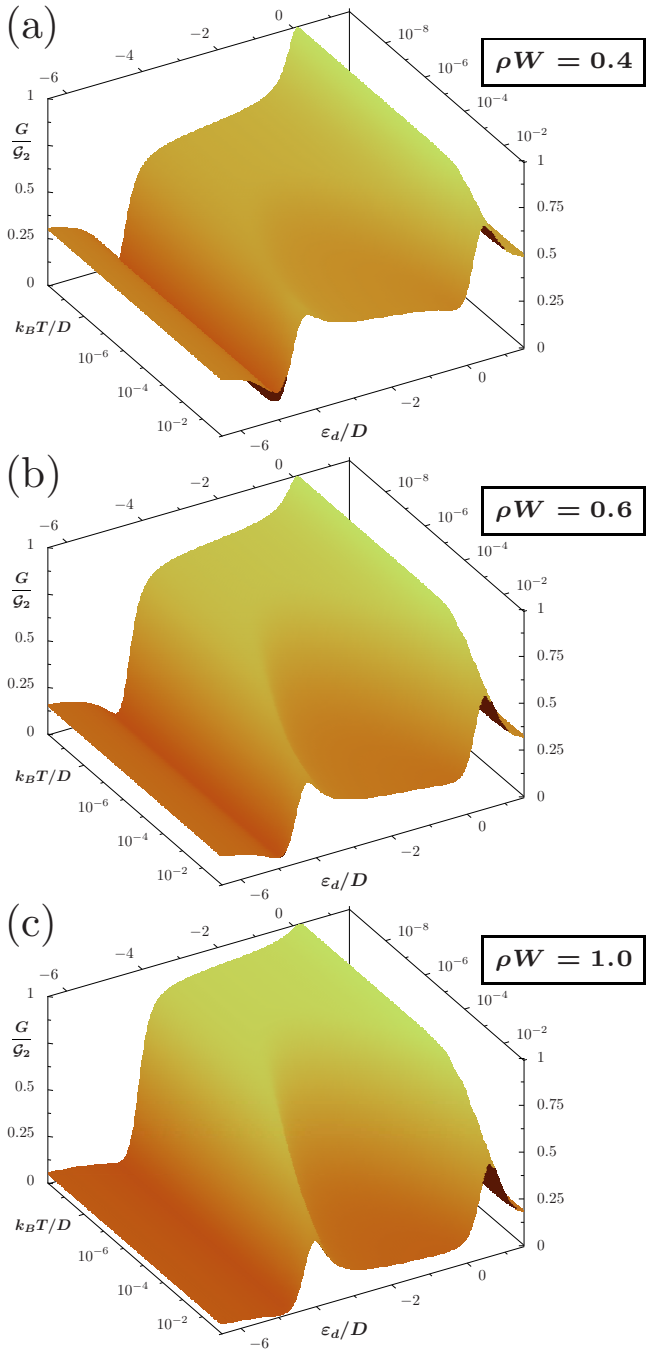

FIG. 5. (Color online) Conductance as a function of the temperature and dot-level energy for $U=5D$, $\Gamma_w=0.15D$, and the indicated wire potentials W. In the Kondo regime, i.e., between the $\Delta_2^*=0$ and the $\Delta_0^*=0$ resonances, as ρW grows, the Coulomb-blockade region evolves into a valley, while at low temperatures the conductance rises toward a ballistic Kondo plateau. Outside the Kondo regime, the conductance approaches zero. Overall, the large-ρW landscape reproduces the temperature and dot-level dependence of the conductance through a single-electron transistor.

reversed to the Kondo-valley landscape displayed in Fig. 3.

5. Thermal dependence of the conductance

This section compares the NRG results for the temperature dependence of the conductance with the mapping (6). We fix the parameters $U=5D$ and $\Gamma_w=0.15D$, and consider seven gate potentials applied to the wire: $\rho W=0$, 0.1, 0.2, 0.3, 0.4, 0.6, and 1.0. To sample the dot-energy dependence of the data, four plots will be discussed, corresponding to the four dot energies indexed by the vertical arrows in Fig. 2. For each run, the Kondo temperature resulting from the definition $G(T_K)\equiv\mathcal{G}_2/2$ and the ground-state phase shift calculated[22] from the low-energy eigenvalues of H_A appear in Table I.

Figure 6 shows the thermal dependence of the conductance for $\varepsilon_a=0$ and seven gate potentials ρW. As the potential grows from $\rho W=0$ to $\rho W=1$ and the ground-state phase shift, described by the circles in Fig. 2, decreases from $\pi/2$ to nearly zero, the conductance $G(T)$ evolves from monotonically increasing to monotonically decreasing. In all cases, the model Hamiltonian lying well within the Kondo regime, the agreement with the solid curves representing Eq. (6) is excellent.

Figure 7 displays temperature-dependent conductances for $\varepsilon_d=-3.4D$. The other model parameters are those in Fig. 6. As Table I shows, the dot-Hamiltonian asymmetry makes each ground-state phase shift somewhat larger than the corresponding δ in Fig. 6. With the exception of the open circles, which vanish (reach the quantum limit) at low (high) temperatures in Fig. 6 and can only move up (down) in response to the particle-hole asymmetry, Eq. (8c) [Eq. (8d)] pushes down (up) the low (high) temperature conductances. The Kondo temperatures are now spread over a wider ranger. Apart from such minor changes, however, Figs. 6 and 7 display the same picture. In particular, all Hamiltonians and temperatures being in the Kondo regime, the agreement with Eq. (6) is flawless.

As indicated by the solid lines in Fig. 2, for $\rho W=0$, the borders of the Kondo regime lie near $|\varepsilon_a|=U/2-\Gamma$. With $\varepsilon_d=-4D$, i.e., $\varepsilon_a=-1.5D$, our model Hamiltonian is still within the Kondo regime. As ρW grows, however, the Kondo regime is shifted toward higher ε_d. The Kondo regime is centered at $\varepsilon_a=0$. As ρW grows, the Kondo regime is uniformly shifted toward higher dot energies. It results that the open and filled triangles in Fig. 8, which represent conductances for $\rho W=0.8$ and 1, respectively, correspond to Hamiltonians in the mixed-valence regime. While the other curves, computed for smaller ρW's and hence still within or nearly within the Kondo regime, agree with Eq. (6), the deviations separating the triangles from the solid lines at high temperatures, $k_BT\gtrsim 10^{-2}D$, are substantial. The discrepancies are reminders that, in the mixed-valence regime, the dominant characteristic energy is $\mathcal{E}_c^{mv}=\Gamma_w$, which restricts the domain of Eq. (6) to $k_BT\ll\Gamma_w=0.15D$. Our numerical study of the embedded configuration reported similar deviations.[22] Given that the conductance curves cross the $G=\mathcal{G}_2/2$ horizontal at relatively high temperatures, in the nonuniversal thermal range $k_BT\lesssim\Gamma_w$, it would be inappropriate to extract Kondo temperatures from the identification $G(T/T_K)=\mathcal{G}_2/2$; each of the two T_K's marked with asterisks in Table I was therefore adjusted to make the corresponding solid line run through a triangle near $G=0.7\mathcal{G}_2$.

Since the wire potential displaces the Kondo regime to higher dot energies, for $\varepsilon_d\to 0$ we expect the $\rho W=0$ Hamiltonian to leave the Kondo regime before the $\rho W>0$ Hamil-

TABLE I. Phase shifts and Kondo temperatures for the 32 NRG runs depicted in Figs. 6–9. The ground-state phase shifts δ come from the low-energy spectrum of the model Hamiltonian, and the Kondo temperatures, from the definition $G(T=T_K)\equiv\mathcal{G}_2/2$. The Kondo temperature marked with an asterisk belongs to a Hamiltonian in the mixed-valence regime and, as explained in the text, had to be obtained by matching the solid lines to conductances computed at temperatures below T_K.

Figure	Symbol	ρW	δ/π	k_BT_K/D	Symbol	ρW	δ/π	k_BT_K/D
6	○	0.00	0.50	8.1×10^{-7}	●	0.10	0.40	8.6×10^{-7}
6	□	0.20	0.32	1.0×10^{-6}	■	0.30	0.26	1.3×10^{-6}
6	◇	0.40	0.22	1.6×10^{-6}	◆	0.60	0.16	2.5×10^{-6}
6	△	0.80	0.13	3.8×10^{-6}	▲	1.00	0.11	6.0×10^{-6}
7	○	0.00	0.51	4.4×10^{-6}	●	0.10	0.41	5.9×10^{-6}
7	□	0.20	0.33	8.9×10^{-6}	■	0.30	0.27	1.4×10^{-5}
7	◇	0.40	0.23	2.2×10^{-5}	◆	0.60	0.17	5.7×10^{-5}
7	△	0.80	0.15	1.4×10^{-4}	▲	1.00	0.13	3.6×10^{-4}
8	○	0.00	0.52	8.9×10^{-5}	●	0.10	0.43	1.4×10^{-4}
8	□	0.20	0.35	2.5×10^{-4}	■	0.30	0.29	4.5×10^{-4}
8	◇	0.40	0.25	9.6×10^{-4}	◆	0.60	0.22	3.0×10^{-3}
8	△	0.80	0.22	$1.0\times10^{-2*}$	▲	1.00	0.25	$1.2\times10^{-2*}$
9	○	0.00	0.42	7.6×10^{-3}	●	0.10	0.34	4.5×10^{-3}
9	□	0.20	0.27	2.7×10^{-3}	■	0.30	0.21	2.0×10^{-3}
9	◇	0.40	0.17	1.4×10^{-3}	◆	0.60	0.12	6.6×10^{-4}
9	△	0.80	0.09	3.5×10^{-4}	▲	1.00	0.08	1.9×10^{-4}

tonians. Accordingly, Fig. 9 contrasts triangles and squares very well fitted by Eq. (6) with circles and diamonds that depart significantly from the solid lines representing the universal mapping for $k_BT>3\times10^{-2}D$.

The ground-state phase shift δ decreases with ε_d. Thus, while the phase shifts that Table I associates with each ρW in Fig. 7 and 8 exceed the phase shift for the same ρW in Fig. 6, the phase shift for each wire potential in Fig. 9 is smaller than the corresponding phase shift in Fig. 8. In compliance with Eq. (8c), each low-temperature conductance in Fig. 9 is larger than the corresponding conductance in Fig. 8. This comparison cannot be extended to the high-temperature regime because the Kondo temperatures derived from the filled triangles and diamonds in Figs. 8 and 9 are so high that even the right extreme of the temperature axis violates the condition $T\gg T_K$ in Eq. (8d).

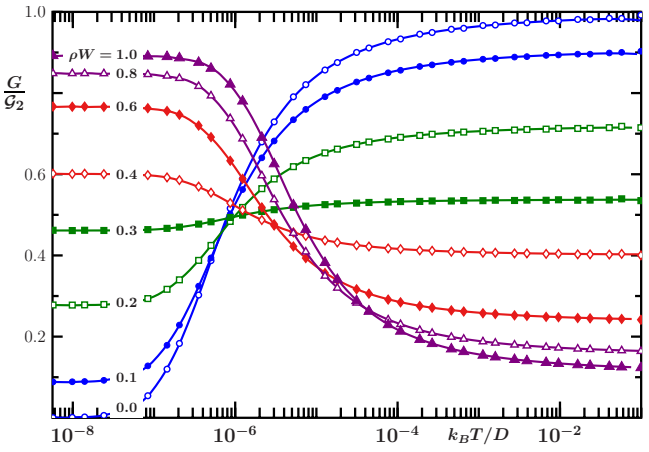

FIG. 6. (Color online) Temperature dependence of the conductance for $U=5D$, $\Gamma_w=0.15D$, $\varepsilon_d=-2.5D$, and the displayed wire potentials W. The symbols depict results of NRG runs. The solid curves through them represent Eq. (6) with δ computed from the low-energy eigenvalues of the model Hamiltonian, and T_K, from the definition $G(T=T_K)=\mathcal{G}_2/2$. For $W=0$, the model Hamiltonian reduces to the symmetric Hamiltonian, and the conductance is complementary to the universal conductance curve, $G(T/T_K)=\mathcal{G}_2-G^S(T/T_K)$. For larger wire potentials, the ground-state phase shift grows, but since the model Hamiltonian remains in the Kondo regime, the agreement with the solid lines is excellent.

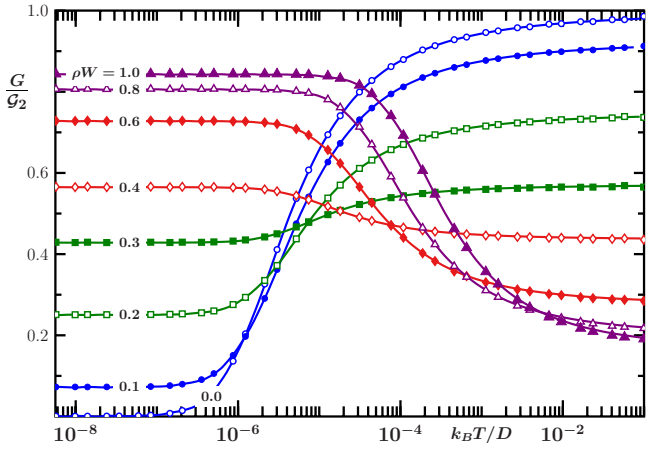

FIG. 7. (Color online) Analogous to Fig. 6, with $\varepsilon_d=-3.4D$. The particle-hole asymmetry, here more pronounced than in Fig. 6, reduces the conductance at high temperatures and enhances it at low temperatures. Since the model Hamiltonian for each W lies in the Kondo regime, the agreement with Eq. (6) is again excellent.

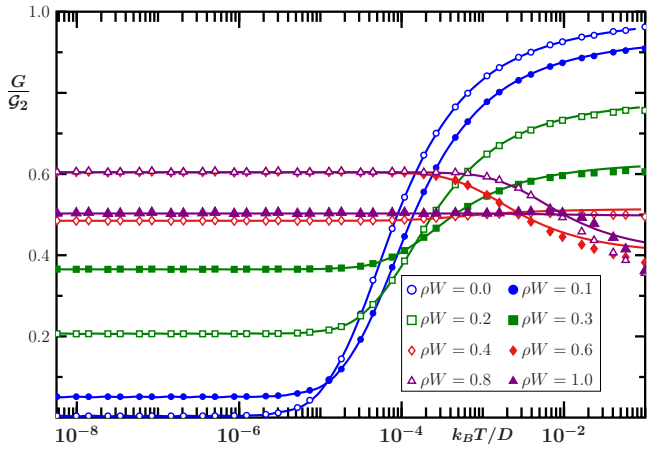

FIG. 8. (Color online) Analogous to Figs. 6 and 7, for $\varepsilon_d = -4.0D$. Four of the curves, those with $\rho W \leq 0.4$, belong to model Hamiltonians in the mixed-valence regime, which restricts Eq. (6) to the temperature range $k_BT \ll \Gamma_w$. For $k_BT > 10^{-2}D$, the diamonds and triangles therefore show disagreement with the solid lines. The disagreement grows with W because the wire gate potential pushes the Hamiltonian away from the Kondo regime.

B. Results for $U < D$

We will now present conductances calculated with $U = 0.05D$, a parameter 100 times smaller than the Coulomb repulsion in Sec. IV A. The reduction pushes the Kondo regime to lower temperatures to make room for a new domain at thermal energies $k_BT \approx 0.05D$, in which the $n_d = 0$ and $n_d = 2$ dot occupations are thermally accessible. The conductance being unchanged in the Kondo regime, the following discussion will focus on the modifications at higher temperatures.

1. Conductance for $W = 0$

Figure 10, analogous to Fig. 3, shows the conductance as a function of the temperature and of the dot energy for dot-level width $\Gamma = 2 \times 10^{-3}D$ and no wire gate potential. At high temperatures, all dot occupations are thermally accessible, and the model Hamiltonian is in the free dot-orbital regime.[24] In the absence of Kondo screening, the dot is effectively decoupled from the wire, through which currents can flow ballistically under external biases. The zero-bias conductance is therefore unitary.

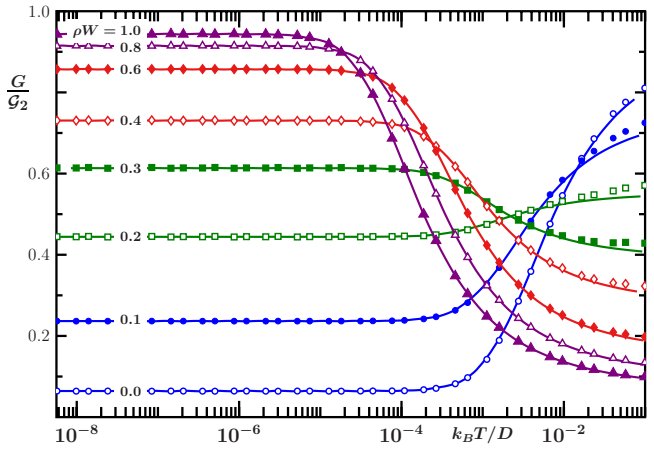

FIG. 9. (Color online) Analogous to Figs. 6–8, for $\varepsilon_d = 0.4D$. With $\varepsilon_d + U/2 > 0$, the (positive) wire potential tends to dampen the effects of particle-hole asymmetry. For $\rho W \leq 0.3D$, the model Hamiltonian now lies in the mixed-valence regime, and the calculated conductances deviate significantly from the solid lines in the temperature range $k_BT > 10^{-2}D$.

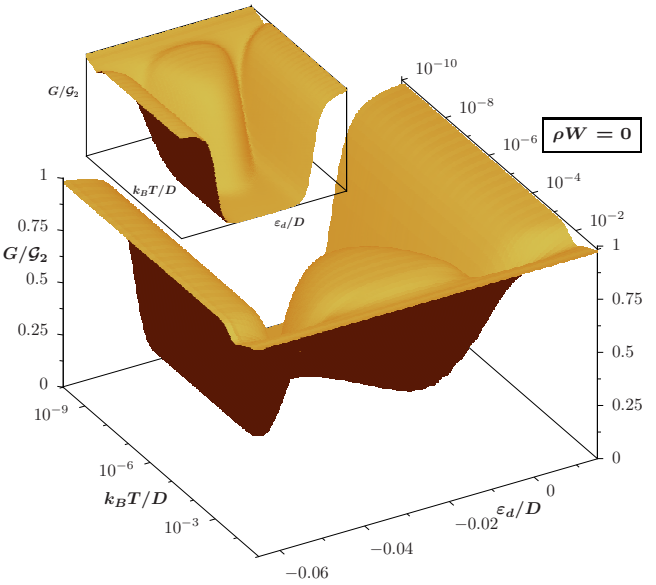

FIG. 10. (Color online) Conductance as a function of the temperature and dot-level energy for $W = 0$, $U = 0.05D$, and $\Gamma = 2 \times 10^{-3}D$. The inset shows the same plot from the opposite viewpoint, so that the temperature decays toward the viewer, instead of rising. The invariance of the Hamiltonian under a particle-hole transformation makes the plot symmetric with respect to the $\varepsilon_d + U/2 = 0$ plane. At high temperatures, with $k_BT > U$, all occupations of the dot orbital are thermally accessible, and conduction through the wire is ballistic. As the temperature is lowered in the Kondo (mixed-valence) regime, the conductance drops gradually (sharply) to zero, because the coupling to the quantum dot obstructs conduction through the wire.

As the temperature is lowered, the more energetic dot occupations n_d are frozen out. Since the dot energies for $n_d = 0$, 1, and 2 are 0, ε_d, and $2\varepsilon_d + U$, respectively, depending on the dot energy the model Hamiltonian will be driven to a domain in which the dot occupation is close to 0 or 2 (the nonmagnetic regime), close to 1 (the Kondo regime), or a fractional number between 0 and 1 or between 1 and 2 (the mixed-valence regime).

The crossover to any of these from the free-orbital regime occurs at thermal energies approximately equal to dot-charge excitation energies. The crossover from the free-orbital regime to the Kondo regime, for instance, takes place at temperatures $k_BT \lesssim U$, approximately equal to the charge-excitation energies $\Delta_0 = |\varepsilon_d|$, from the $n_d = 1$ to the $n_d = 0$ dot configurations, and $\Delta_2 = \varepsilon_d + U$, from the $n_d = 1$ to the $n_d = 2$ configurations. The crossover coincides, in other words, with the charge-excitation resonances that enhance the dot-level spectral density and hence the coupling between the dot and the wire.[31] Since the coupling obstructs the flow of electrons through the wire, the conductance dips at the crossover. The

trough running parallel to the ε_d axis at $k_BT \approx 1 \times 10^{-2}$ in Fig. 10 thus marks the crossover from the free-orbital to the nonmagnetic, mixed-valence, or Kondo regimes. Once the Hamiltonian is over the trough on its journey toward $T=0$, only the temperature shift distinguishes the landscape in Fig. 10 from the plot in Fig. 3.

2. Conductance for weak scattering potentials

Compare next Fig. 11, which shows the conductance as a function of the temperature and dot energy for $\Gamma_w = 2 \times 10^{-3} D$ and three small wire potentials, with Fig. 4. Again, the differences direct our attention to the high-temperature end of the plot.

Even though the dot is decoupled from the conduction band at high temperatures, the wire gate potential reduces the conductance, because the charge induced by the potential on the wire partially blocks the flow of electrons. The induced charge being $2\delta_w/\pi$, we expect the conduction to be a function of δ. In fact, the conductance of one-dimensional electrons phase shifted by δ_w is $G = \mathcal{G}_2 \cos^2 \delta_w$,[22] an expression that can be compared with the conductance in the Kondo regime for $T \gg T_K$: if $\varepsilon_d = -U/2$, the ground-state phase shift is $\delta = \pi/2 + \delta_w$, and so the conductance on the right-hand side of Eq. (8d) is $\mathcal{G}_2 \cos^2 \delta$.

On the symmetric plane $\varepsilon_d = -U/2$, therefore, in the free-orbital regime and at the highest temperatures in the Kondo regime, the conductance must be the same. For small wire potentials, as in Fig. 10, the two regimes are separated by a trough. As the potential grows, the trough progressively evolves into a ridge, following pari passu the emergence of a Kondo plateau out of the Kondo valley at low temperatures. The latter transformation is a feature of the Kondo regime; we have already seen it in Fig. 4 and discussed it in Sec. IV A 3.

Closer inspection of the temperature range $k_BT > 0.01D$ in Fig. 11(c) shows that the trough and the ridge coexist. The former is visible in the left-hand half of the plot ($\varepsilon_d < -U/2$), the latter, in the right-hand half ($\varepsilon_d > -U/2$). The coexistence identifies interference between the currents through the dot and the wire. This is the same phenomenon discussed in Sec IV A 3, which here likewise originates the antiresonance profile on the $k_BT = 1 \times 10^{-10} D$ plane, at the rear. At high temperatures the interference is much less pronounced, because the maxima of the dot spectral density at the charge-excitation energies $\epsilon = \Delta_0$ and $\epsilon = \Delta_2$, which account for the ridge and the trough, are much weaker than the maximum of the spectral density at the Kondo resonance.[31,32]

3. Conductance for strong scattering potentials

Figure 12 shows the conductance as a function of the temperature and dot energy for $\Gamma_w = 2 \times 10^{-3} D$ and three wire gate potentials, $\rho W = 0.4$, 0.6, and 1. Under the stronger potentials, a fully developed ridge marks the crossover between the free-orbital and the three lower-temperature regimes. Behind the ridge, i.e., for $k_BT \ll U$, the three landscapes are similar to the ones in Fig. 5.

Sec. IV A 4 showed that, in the large wire-potential limit, the conductance for the side-coupled geometry approaches the conductance for the embedded geometry with $W=0$. We therefore expect the sequence in Fig. 12 to approach the conduction landscape for the Anderson model of a single-electron transistor (SET) (Refs. 17 and 33) for the same level width and no wire gate potential, i.e., to approach the plot in

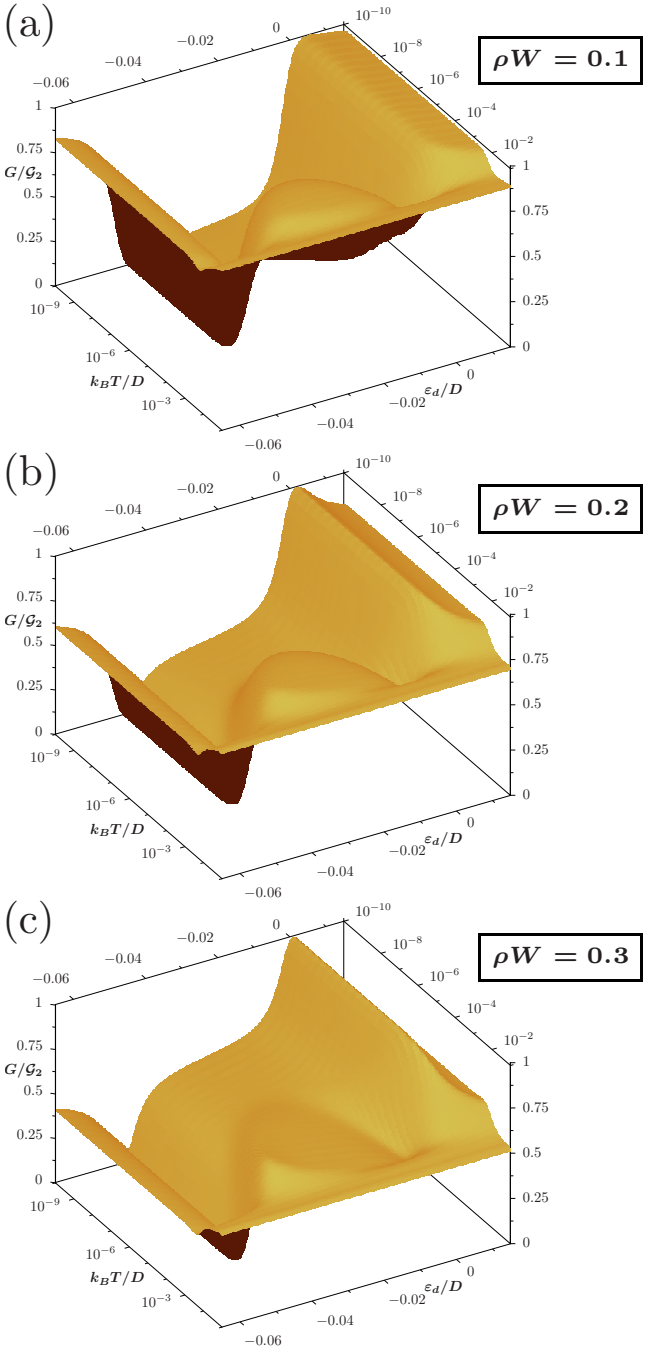

FIG. 11. (Color online) Conductance as a function of the temperature and dot-level energy for $U = 0.05D$, $\Gamma_w = 2 \times 10^{-3} D$, and the displayed wire gate potentials W. At high temperatures, as in Fig. 10, the wire is effectively decoupled from the quantum dot; only the wire potential obstructs conduction. As the temperature is decreased for fixed ε_d, a trough at $k_BT \approx U$ marks the crossover to the Kondo, mixed-valence, or even-n_d regimes. In these three regimes, the landscapes (a), (b), and (c) reproduce the dominant features of Figs. 4(a)–4(c), respectively.

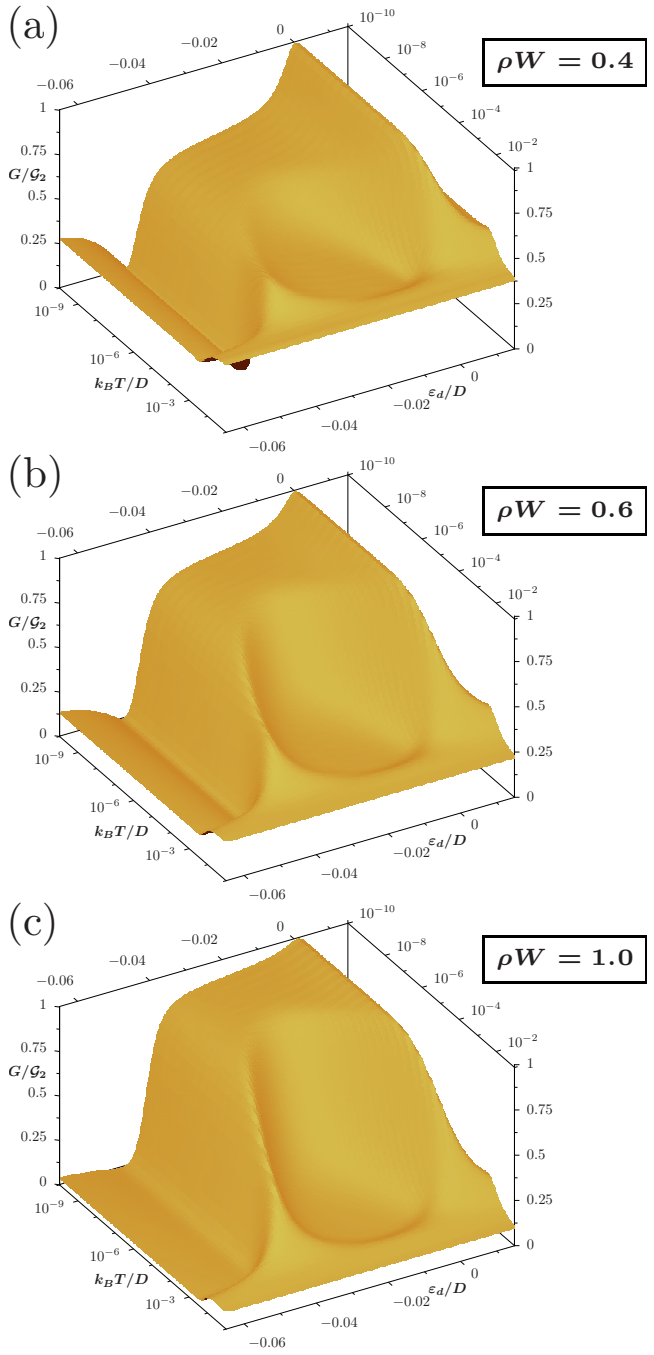

FIG. 12. (Color online) Conductance as a function of the temperature and dot-level energy for $U=0.05D$, $\Gamma_w=2\times10^{-3}D$, and the displayed wire gate potentials W. At high temperatures, as in Fig. 10, the wire is effectively decoupled from the quantum dot, and the conductance depends only on the wire potential. In the temperature range $k_BT\lesssim U$, a ridge that rises with the wire potential marks the crossover from the free-orbital high-temperature domain into the Kondo, mixed-valence, or even-n_d regimes. In these lower-temperature regimes, the landscapes (a), (b), and (c) are similar to the ones in Figs. 5(a)–5(c), respectively.

Fig. 13(a) of Ref. 22. Compared to that plot, Fig. 12(c) confirms that the conductances computed for $\rho W=1$ are very close to the SET conductances. In particular, the ridge at high

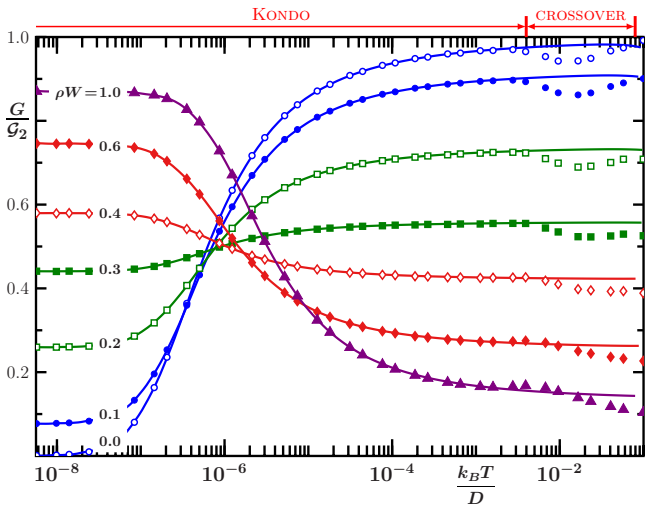

FIG. 13. (Color online) Temperature dependence of the conductance for $U=0.05D$, $\Gamma_w=2\times10^{-3}D$, $\varepsilon_d=-0.03D$, and the seven displayed wire potentials W. The symbols result from NRG runs. The solid lines through them represent Eq. (6), with Kondo temperature T_K such that $G(T_K)=\mathcal{G}_2/2$ and phase shift δ extracted from the low-energy spectrum of the model Hamiltonian. The arrows above the top horizontal axis stake out the Kondo regime, in which the symbols stick to the solid lines, and its crossover to the free-orbital regime, in which Eq. (6) overestimates the conductance.

temperatures and the flat Kondo plateau at $T\ll T_K$ are signatures of the SET landscape for $U<D$.

4. Thermal dependence of the conductance

Figure 13 shows the cut of each landscape in Figs. 11–13 along the $\varepsilon_d=-0.030D$ plane and compares it with Eq. (6). At high temperatures, the two charge-excitation energies $\Delta_0=0.03D$ and $\Delta_2=0.02$ control the renormalization-group flow of the model Hamiltonian. For $k_BT\gg\Delta_0$, the Hamiltonian is in the free-orbital regime, and all dot occupations are thermally accessible. In the crossover range $\Delta_2\lesssim k_BT\lesssim\Delta_0$, marked by the two-headed arrow above the top horizontal axis in the illustration, the two charge-excitation resonances modulate the conductance. Finally, as k_BT becomes small in comparison with Δ_2, the Hamiltonian enters the Kondo regime, indicated by the single-headed horizontal arrow at the top.

In the free-orbital regime, the conductance is approximately constant, $G\approx\mathcal{G}_2\cos^2\delta_w$. If the wire potential is weak (strong), the conductance initially dips (rises) as the temperature drops into the crossover region, a change that originates the troughs (ridges) in Figs. 10, 11(a), and 11(b) [Figs. 11(c) and 12]. In the crossover, consequently, the conductance departs substantially from Eq. (6). As the temperature drops further and enters the Kondo regime, however, the symbols exhibit excellent agreement with Eq. (6).

The high-temperature troughs (ridges) in Figs. 10, 11(a), and 11(b) (Fig. 12) correspond to the dips (mounds) around $k_BT=1\times10^{-2}D$ drawn by the open and filled circles and squares (filled diamonds and triangles) in Fig. 13. Below $k_BT=1\times10^{-4}D$, in the Kondo regime, the agreement be-

tween the symbols and the solid lines representing Eq. (6) is excellent.

V. COMPARISON WITH EXPERIMENT

A number of experimental studies of transport in T-shaped devices are found in the literature, with which the results reported in Figs. 3–5 can be compared. Figure 1(c) in Ref. 13, which show low-temperature conductance profiles for various level widths, exhibits valleys, plateaus, resonances, and antiresonances—the features found in the low-temperature profiles delineated on the $k_BT=10^{-10}D$ planes in Figs. 3–5. Other publications offer additional examples.[12,19]

Particularly illustrative is the experimental demonstration in Ref. 19, that a gate potential applied to a quantum wire side-coupled to a quantum dot controls the amplitude for transport along the wire relative to that through the dot. Figure 5 in that publication documents the evolution of a low-temperature Kondo valley, characteristic of conduction through the wire, into a low-temperature Kondo plateau, characteristic of conduction through the dot, under a steadily increasing gate potential applied to the wire. Viewed in from Fig. 3 to Fig. 5(c), the landscapes in Sec. IV display the same evolution. The universal mapping (6) qualitatively describes the experimental conductance profiles.

What is more important, the mapping describes quantitatively the thermal dependence of measured conductances. For an illustration, see Fig. 3 in Ref. 21, which fits the temperature-dependence conductances resulting from two gate potentials applied by Sato *et al.*[13] to a T-shaped device. A background current being detected, three parameters were involved in the fit to the first conductance curve: the background conductance, the phase shift, and the Kondo temperature T_K. The same first two parameters and a different Kondo temperature then fitted the second curve. In each case, within the dispersion of the experimental data, optimum agreement resulted.

VI. CONCLUSIONS

Equation (6) offers a unifying view of electrical conduction through a quantum wire side coupled to a quantum dot. Valid over the entire Kondo regime, it captures with error $\mathcal{O}(k_BT/D)$ the conductance crossover from local-moment regime $T \gg T_K$, equivalent to a conduction band weakly interacting with the dot magnetic moment, to the low-temperature regime $T \ll T_K$, in which the dot electron and the conduction electrons around it lock into a singlet making the spectrum of the model Hamiltonian equivalent to a phase-shifted conduction band. The thermal dependence of the conductance is controlled by the phase shift. For $\delta \approx \pi/2$, an approximate equality enforced by the Friedel sum rule in the absence of a wire potential, the formation of the Kondo cloud lowers the conductance from nearly ballistic to nearly zero. A (positive) gate potential applied to the wire induces electric charge that reduces the ground-state phase shift. As ρW pushes δ past $\pi/4$, the conductance curve becomes flat and then reverses the pattern displayed in Fig. 3: for large ρW [Fig. 5(c)], the T-shaped device becomes indistinguishable from a single-electron transistor.[22] For small ρW, by contrast, the landscapes are complementary because the conductance through the single-electron transistor is virtually insensitive to the gate potential applied to the wire.[22]

The Friedel sum rule explains the incongruent responses of the two devices to the external potential. In the embedded configuration of the single-electron transistor, the dot charge n_d controls the conductance. Were it not for the reduction $\Gamma \to \Gamma_w$ and the shifts $\Delta_0 \to \Delta_0^*$, $\Delta_2 \to \Delta_2^*$ that it imposes on the dot-level width and resonance energies, respectively, the wire potential would not affect n_d. As it follows, the wire potential changes the Kondo temperature, but has otherwise no effect upon the thermal dependence of the conductance. Mathematically, this implicit dependence is expressed by the Friedel sum rule $n_d=2(\delta-\delta_w)/\pi$, which relates the dot occupation to the extra charge in the Kondo droplet, i.e., the wire charge measured from the charge induced by the wire potential. In accord with this notion, the mapping between the conductance and the universal function $G^S(T/T_K)$ is parametrized by the phase-shift difference $\delta-\delta_w$ and hence insensitive to the wire potential.[22]

By contrast, the wire potential affects the conductance for the device in Fig. 1 in two direct ways. First, the total charge in the ϕ_0 orbital, i.e., the charge induced by the wire potential plus, at low temperatures, the charge in the Kondo droplet, obstructs the transport of charge through the central portion of the wire. Second, the potential couples c_d to states orthogonal to ϕ_0 and thus opens a conduction path through the quantum dot. For very (strong) weak potentials, the path through ϕ_0 (c_d) is dominant; the landscape in Fig. 3 [Fig. 5(c)] is thus complementary (very similar) to the landscape for a single-electron transistor.[22] For intermediate potentials—see, e.g., Fig. 4(c)—the interference between the currents along the two paths makes the landscape markedly asymmetric in the mixed-valence region, and the availability of two alternate conduction paths, one efficient at low temperatures, the other efficient at high temperatures, makes the landscape remarkably flat in the Kondo regime. According to the Friedel sum rule, the wire charge is $2\delta/\pi$. Much as the dot charge $n_d=2(\delta-\delta_w)/\pi$, which controls conduction in the embedded configuration, parametrizes the mapping to the conductance through the single-electron transistor,[22] the wire charge $2\delta/\pi$ controls conduction in the side-coupled configuration and parametrizes the mapping (6). While the dependence on the dot charge practically shields the conductance for the single-electron transistor from gate potentials applied to the wire, the dependence on the wire charge makes the conductance for the T-shaped device remarkably sensitive to such potentials.

The practical value of universality has been demonstrated in both experimental arrangements. In the embedded configuration, early in the history of such devices, the universal function $G^S(T/T_K)$ guided the interpretation of conductance data for single-electron transistors.[33] In the side-coupled arrangement, Eq. (6) was shown to fit conductance curves generated in the laboratory[13,19] accurately enough to determine the Kondo temperature and ground-state phase shift within deviations set by the dispersion of the experimental data.

Neither the universal mapping (6), nor the corresponding expression for the embedded configuration[22] determine ex-

plicitly any of the model parameters, let alone the physical constants emulated by the model Hamiltonian. They do offer indirect information that may assist future *ab initio* descriptions of the physical properties of single-electron transistors or *T*-shaped devices. The two mappings of the Kondo-regime conductances to the universal function G^S redefine the ultimate target of such *ab initio* problems, from conductance curves to phase shifts and Kondo temperatures. In a less challenging arena, they bring Kondo-regime conductance curves within the reach of the Bethe-*ansatz* approach.[34,35] Additionally, on the basis of the experience with thermodynamical properties,[36,37] we also expect the mappings to offer benchmarks to check the accuracy of numerically or analytically computed transport properties for model Hamiltonians describing quantum-dot arrays.

ACKNOWLEDGMENT

This work was supported by the CNPq and FAPESP.

*Present address: Instituto de Física, Universidade Federal Fluminense, Niterói 24210-346, RJ, Brazil.

[1] W. Hofstetter, J. König, and H. Schoeller, Phys. Rev. Lett. **87**, 156803 (2001).
[2] H. Aikawa, K. Kobayashi, A. Sano, S. Katsumoto, and Y. Iye, Phys. Rev. Lett. **92**, 176802 (2004).
[3] A. Aharony, O. Entin-Wohlman, T. Otsuka, S. Katsumoto, H. Aikawa, and K. Kobayashi, Phys. Rev. B **73**, 195329 (2006).
[4] A. Fuhrer, P. Brusheim, T. Ihn, M. Sigrist, K. Ensslin, W. Wegscheider, and M. Bichler, Phys. Rev. B **73**, 205326 (2006).
[5] L. G. G. V. Dias da Silva, N. P. Sandler, K. Ingersent, and S. E. Ulloa, Phys. Rev. Lett. **97**, 096603 (2006).
[6] L. G. G. V. Dias da Silva, K. Ingersent, N. Sandler, and S. E. Ulloa, Phys. Rev. B **78**, 153304 (2008).
[7] B. R. Bułka and P. Stefański, Phys. Rev. Lett. **86**, 5128 (2001).
[8] A. A. Clerk, X. Waintal, and P. W. Brouwer, Phys. Rev. Lett. **86**, 4636 (2001).
[9] M. E. Torio, K. Hallberg, A. H. Ceccatto, and C. R. Proetto, Phys. Rev. B **65**, 085302 (2002).
[10] R. Franco, M. S. Figueira, and E. V. Anda, Phys. Rev. B **67**, 155301 (2003).
[11] I. Maruyama, N. Shibata, and K. Ueda, J. Phys. Soc. Jpn. **73**, 3239 (2004).
[12] K. Kobayashi, H. Aikawa, A. Sano, S. Katsumoto, and Y. Iye, Phys. Rev. B **70**, 035319 (2004).
[13] M. Sato, H. Aikawa, K. Kobayashi, S. Katsumoto, and Y. Iye, Phys. Rev. Lett. **95**, 066801 (2005).
[14] R. Žitko and J. Bonča, Phys. Rev. B **73**, 035332 (2006).
[15] I. Maruyama, N. Shibata, and K. Ueda, Physica B **378-380**, 938 (2006).
[16] S. Katsumoto, J. Phys.: Condens. Matter **19**, 233201 (2007).
[17] D. Goldhaber-Gordon, H. Shtrikman, D. Mahalu, D. Abusch-Magder, U. Meirav, and M. A. Kastner, Nature (London) **391**, 156 (1998).
[18] T. Costi, A. Hewson, and V. Zlatic, J. Phys.: Condens. Matter **6**, 2519 (1994).
[19] S. Katsumoto, M. Sato, H. Aikawa, and Y. Iye, Physica E **34**, 36 (2006).
[20] P. S. Cornaglia and D. R. Grempel, Phys. Rev. B **71**, 075305 (2005).
[21] A. C. Seridonio, M. Yoshida, and L. N. Oliveira, Europhys. Lett. **86**, 67006 (2009).
[22] M. Yoshida, A. C. Seridonio, and L. N. Oliveira, preceding paper, Phys. Rev. B **80**, 235317 (2009).
[23] F. D. M. Haldane, Phys. Rev. Lett. **40**, 416 (1978).
[24] H. R. Krishna-murthy, J. W. Wilkins, and K. G. Wilson, Phys. Rev. B **21**, 1003 (1980).
[25] H. R. Krishna-murthy, J. W. Wilkins, and K. G. Wilson, Phys. Rev. B **21**, 1044 (1980).
[26] R. Bulla, T. A. Costi, and T. Pruschke, Rev. Mod. Phys. **80**, 395 (2008).
[27] D. C. Langreth, Phys. Rev. **150**, 516 (1966).
[28] L. I. Glazman and M. E. Raikh, JETP Lett. **47**, 452 (1987).
[29] T. K. Ng and P. A. Lee, Phys. Rev. Lett. **61**, 1768 (1988).
[30] U. Fano, Phys. Rev. **124**, 1866 (1961).
[31] A. C. Hewson, *The Kondo Problem to Heavy Fermions* (Cambridge University Press, Cambridge, England, 1993).
[32] H. O. Frota and L. N. Oliveira, Phys. Rev. B **33**, 7871 (1986).
[33] D. Goldhaber-Gordon, J. Göres, M. A. Kastner, H. Shtrikman, D. Mahalu, and U. Meirav, Phys. Rev. Lett. **81**, 5225 (1998).
[34] N. Andrei, K. Furuya, and J. H. Lowenstein, Rev. Mod. Phys. **55**, 331 (1983).
[35] A. M. Tsvelick and P. B. Wiegmann, Adv. Phys. **32**, 453 (1983).
[36] J. B. Silva, W. L. C. Lima, W. C. Oliveira, J. L. N. Mello, L. N. Oliveira, and J. W. Wilkins, Phys. Rev. Lett. **76**, 275 (1996).
[37] V. L. Campo, Jr. and L. N. Oliveira, Phys. Rev. B **70**, 153401 (2004).